Birefringent Field-Modulation Imaging of Transparent Ferroelectrics

Yohei Uemura ,[1,*] Satoshi Matsuoka ,[1] Jun'ya Tsutsumi ,[2] Sachio Horiuchi ,[2] Shunto Arai ,[1] and Tatsuo Hasegawa [1]

[1] *Department of Applied Physics, The University of Tokyo, Tokyo 113-8656, Japan*
[2] *Research Institute for Advanced Electronics and Photonics (RIAEP), National Institute of Advanced Industrial Science and Technology (AIST), Tsukuba, Ibaraki 305-8565, Japan*

(Received 30 April 2020; revised 9 July 2020; accepted 17 July 2020; published 21 August 2020)

Observations of ferroelectric domains and domain walls are essential for understanding ferroelectric switching characteristics. Here, we demonstrate that the use of optical birefringence, coupled with a first-order electro-optic effect (Pockels effect), allows the visualization of ferroelectric domains in transparent ferroelectric materials. We utilize a field-modulation imaging technique, with the use of a complementary metal-oxide-semiconductor (CMOS) area image sensor to detect slight differences in parallel- and crossed-Nicols polarized optical microscopy images between forward- and reverse-electric-field applications. The ferroelectric domains with antiparallel polarizations are clearly discriminated from each other by the sign of the ellipticity modulation of outgoing elliptically polarized light. The observed images are consistent with piezoresponse force microscopy images of transparent single-crystal films of 2-methylbenzimidazole (MBI). The modulation signal at both polarization configurations exhibit clear sign changes in the wavelength dispersion, owing to the anisotropic nature of the MBI films. The unique optical-probe nature also reveals the existence of two types of domain walls with different three-dimensional orientations.

DOI: 10.1103/PhysRevApplied.14.024060

I. INTRODUCTION

Many ferroelectrics, derived either from ceramic or organic materials, are intrinsically optically transparent and do not absorb visible light. This feature is due to the large band-gap energies of the materials [1–3] and is useful for various practical applications. Meanwhile, an extremely large dielectric response and notable switching characteristics, unique to ferroelectrics, originate from the motions of domain walls that divide ferroelectric domains with different orientations of spontaneous polarizations [4,5]. Thus, the examination of ferroelectric domains and domain walls is fundamental to understanding the characteristics of ferroelectrics.

Some of the domain walls in transparent ferroelectrics are visible by optical microscopy, when they involve abrupt changes in the refractive index, which cause slight light scattering around the walls [6–9]. Other domain walls can also become visible by crossed-Nicols polarized microscopy, if the spontaneous polarizations of adjacent domains are *not* antiparallel with each other [10]. In such a case, the respective domains divided by the domain walls can be discriminated by the relative tilt of the optical indicatrix associated with the birefringent nature of the ferroelectrics. These simple optical microscopy observations have significant benefits in the investigation of domain walls and related ferroelectric phenomena. However, the visibility is not sufficient, especially for thin films, because of the short path lengths involved. Furthermore, the method is not applicable for versatile use because it is difficult to observe antiparallel (i.e., 180°) domain walls that do not accompany abrupt changes in the refractive index around the walls, whereas they are the most important and are frequently formed in ferroelectric crystals.

For the observation of ferroelectric domains, other techniques have been developed, such as piezoresponse force microscopy (PFM) [11–14], scanning nonlinear dielectric microscopy [15,16], second-harmonic-generation microscopy [17–19], and terahertz radiation imaging [20–22]. These sophisticated methods take advantage of the piezoelectric, nonlinear dielectric, or nonlinear-optical responses in ferroelectric materials, which do not exhibit inversion symmetry. Recently, we successfully developed a simple optical-microscopy-based technique, named ferroelectrics field-modulation imaging (FFMI) [23,24]. The technique utilizes a slight change in optical absorbance under external electric field (electroabsorption effect) to induce the contrasting of optical microscopy images between neighboring ferroelectric domains with different spontaneous polarization orientations. In this technique,

*uemura@hsgw.t.u-tokyo.ac.jp

a CMOS area image sensor is adopted to detect an induced slight difference in microscopy images between that obtained under the application of a forward electric field and that from reverse-electric-field application, sensitively and collectively over a wide area. We demonstrate that this technique allows for the clear visualization of antiparallel domain walls in ferroelectric thin films of hydrogen-bonded molecular cocrystals (i.e., composed of proton-donor and proton-acceptor molecules) that exhibit an electroabsorption effect, owing to the ionized π-conjugated molecules. However, the FFMI technique, using a nonpolarized microscope, as previously reported, is not applicable to transparent ferroelectrics, because modulation of the optical absorption in the visible range is required for the observation of field-modulation signals.

Here, we demonstrate that the use of optical birefringence in the FFMI technique allows the visualization of ferroelectric domains and domain walls in transparent ferroelectric materials. We introduce parallel- and crossed-Nicols observations into the FFMI technique to detect slight changes in the birefringence of the respective domains under applied electric fields. We first describe the essence of the birefringent FFMI technique in terms of the ellipticity modulation of outgoing elliptically polarized light. The hydrogen-bonded single-component molecular ferroelectrics [25] of 2-methylbenzimidazole (MBI) [26,27], as a target transparent ferroelectric material, presents excellent ferroelectric characteristics at room temperature ($T_c > 400$ K). We demonstrate that the birefringent FFMI enables the clear visualization of domain walls that discriminate the ferroelectric domains with antiparallel (180°) polarizations in the MBI single-crystal thin films. We show that the wavelength dependence of the modulated signal provides clear evidence of ellipticity modulation. We also discuss an advantage of the technique that allows the investigation of the three-dimensional orientations of the domain walls within the MBI films.

II. BIREFRINGENT FERROELECTRIC FIELD-MODULATION IMAGING

Figure 1(a) presents the scheme of the optical setup for the birefringent FFMI measurements, which is composed of an incident-light polarizer (hereafter referred to as a

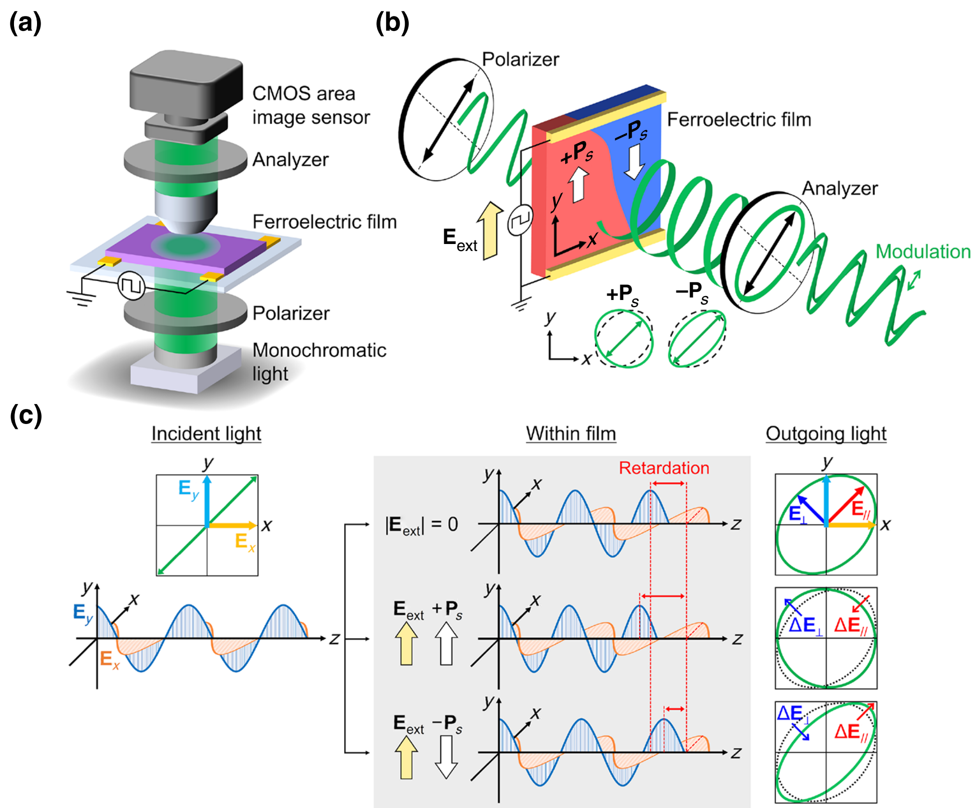

FIG. 1. (a) Scheme for optical setup of birefringent FFMI measurements. (b) Scheme for light polarization state through polarizer, ferroelectric film, and analyzer. Electric field of light is shown as green curves. Pair of green ellipses at the bottom represent variation of outgoing elliptically polarized light under external electric field from respective ferroelectric domains. Dotted black ellipses signify polarized light without external field, and green arrows in the ellipses signify the amplitude of linearly polarized light through the analyzer. (c) Schematics of the outgoing elliptically polarized light without $\mathbf{E}_{ext}$ for the domains with both $+\mathbf{P}_s$ and $-\mathbf{P}_s$ (top), with $\mathbf{E}_{ext}$ on the domain with $+\mathbf{P}_s$ (middle), and with $\mathbf{E}_{ext}$ on the domain with $-\mathbf{P}_s$ (bottom). Antiparallel domains results in different ellipticity of the outgoing elliptically polarized light. Axes of ellipses represent amplitudes of $T_\perp$ and $T_{||}$.

polarizer), a ferroelectric single-crystal film that involves an antiparallel domain wall, and a polarizer after the sample (which we describe as an analyzer). We assume an orthogonal coordinate system, in which the z axis is parallel to the beam path and perpendicular to the film plane, and the y axis is parallel to the direction of spontaneous polarizations in the ferroelectric film, as presented in Fig. 1(b). We set the polarizer angle at 45° from the x axis in order that the amplitudes of the oscillating electric fields along the x and y axes ($\mathbf{E}_x$ and $\mathbf{E}_y$) of incident light would be the same. The phases along the x and y axes are retarded within the ferroelectric film, depending on the refractive indices of n_x and n_y, respectively. Eventually, the outgoing light from the film is elliptically polarized, depending on the difference in phase retardation, ϕ, along the x and y axes, which is expressed as

$$\phi = \frac{2\pi d}{\lambda}(n_y - n_x), \tag{1}$$

where d and λ are the crystal thickness and wavelength, respectively. Because the refractive index, n_y as well as n_x, is the same for both domains with antiparallel spontaneous polarizations ($+\mathbf{P}_s$ and $-\mathbf{P}_s$), the outgoing light has the same ellipticity. This is the reason why the antiparallel domain walls are not visible in the ordinary crossed-Nicols polarized microscopy images.

To consider transmitted light through the entire optical system, we define $\mathbf{E}_{||}$ and $\mathbf{E}_{\perp}$ as the electric field of light through the analyzer that is oriented parallel to and crossed with the polarizer, respectively. $\mathbf{E}_{||}$ and $\mathbf{E}_{\perp}$ correspond to the lengths of the ellipse axes of the elliptically polarized light, as presented in Fig. 1(c). The transmittances through the analyzer oriented parallel to [$T_{||} = |\mathbf{E}_{||}|^2/(|\mathbf{E}_x|^2 + |\mathbf{E}_y|^2)$] and crossed with [$T_{\perp} = |\mathbf{E}_{\perp}|^2/(|\mathbf{E}_x|^2 + |\mathbf{E}_y|^2)$] the polarizer are expressed as a function of ϕ as

$$T_{\parallel} = \cos^2\left(\frac{\phi}{2}\right), \tag{2}$$

$$T_{\perp} = \sin^2\left(\frac{\phi}{2}\right) = 1 - T_{\parallel}. \tag{3}$$

For simplicity, we neglect reflection at the interface.

We assume that the external electric field, $\mathbf{E}_{\rm ext}$, is applied along the y axis, by which the refractive index is modulated, owing to the first-order electro-optic effect (Pockels effect). Because the effect depends on the relative orientations between $\mathbf{P}_s$ and $\mathbf{E}_{\rm ext}$, the change in ϕ due to $\mathbf{E}_{\rm ext}$ is reversed in sign to each other between the domains with antiparallel polarizations. In addition, the intensity of elliptically polarized light ($=|\mathbf{E}_x|^2 + |\mathbf{E}_y|^2$) does not change with $\mathbf{E}_{\rm ext}$, because the amplitudes of $\mathbf{E}_x$ and $\mathbf{E}_y$ do not change. This means that the antiparallel domain walls are not visible in the nonpolarized microscope, even if $\mathbf{E}_{\rm ext}$ is applied. On the contrary, the change in ellipticity with $\mathbf{E}_{\rm ext}$ can be detected as the change in the polarized components of the transmittance [28,29], $\Delta T_{||}$ and $\Delta T_{\perp}$, defined as the difference in transmittance between positive and negative bias. $\Delta T_{||}$ and $\Delta T_{\perp}$ are expressed by the change in the birefringence, Δn, as

$$\Delta T_{\parallel} = \cos^2\left(\frac{\phi}{2} + \frac{\pi d}{\lambda}\Delta n\right) - \cos^2\left(\frac{\phi}{2} - \frac{\pi d}{\lambda}\Delta n\right), \tag{4}$$

$$\Delta T_{\perp} = -\Delta T_{\parallel}, \tag{5}$$

where

$$\Delta n = \frac{\partial(n_y - n_x)}{\partial E}E_{\rm ext}. \tag{6}$$

Thus, the application of $\mathbf{E}_{\rm ext}$ gives the contrast of the microscopy image for domains with antiparallel polarizations, eventually allowing the observation of antiparallel ferroelectric domain walls.

In the actual experiment, we use a measurement system composed of a polarized microscope and a CMOS area image sensor (pco.edge 5.5; PCO AG). We use a light-emitting diode (LED; M660L4; Thorlabs, Inc.) or monochromatized light from a Xe lamp as the light source. A square-wave voltage bias is applied between electrodes to apply forward and reverse electric fields in a direction parallel to the film plane. Polarized microscopy images are captured by the image sensor and are synchronized with the square-wave bias. The spatial distribution of $\Delta T_{||}/T_{||}$ or $\Delta T_{\perp}/T_{\perp}$ in each pixel is collectively processed as a birefringent FFMI image from the captured image. As $\Delta T_{||}/T_{||}$ and $\Delta T_{\perp}/T_{\perp}$ are relatively small ($\sim 10^{-4}$) in the MBI films, the difference image is repeatedly measured and collected to reduce noise.

III. APPLICATION TO TRANSPARENT ORGANIC FERROELECTRIC FILMS

A. Thin-film preparation

We use single-crystal thin films of MBI fabricated by a confined crystal-growth technique, as previously reported [23]. An optical micrograph of the film is shown in Fig. S1 within the Supplemental Material [30]. The films are grown from an N,N-dimethylformamide solution of MBI at 15 wt% concentration between two glass plates (a thicker base plate and a thin cover plate). Stripe-shaped electrodes [line-and-space widths of 50/50 μm and thicknesses of 32 nm (Cr: 2 nm, Au: 30 nm)] are evaporated on the base plate before film growth. After growth, the cover plate is detached from the base plate on which the MBI single-crystal thin films are grown on top of the electrodes. For the facile detachment of the cover plate, we modify

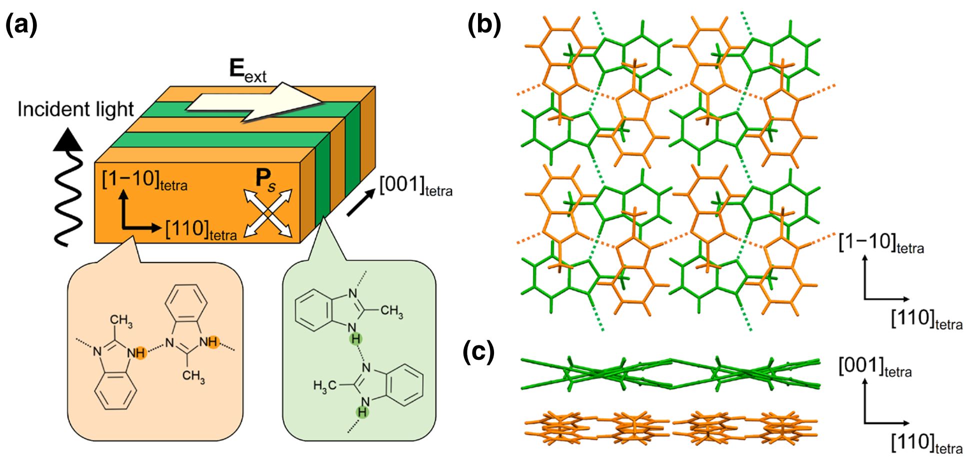

FIG. 2. (a) Crystal orientation of MBI single-crystal thin films. Crystal structure of MBI viewed along (b) $[001]_{tetra}$ and (c) $[1-10]_{tetra}$.

the plate surface using a perfluorinated amorphous polymer layer (Cytop; AGC) to achieve high hydrophobicity. The thickness of the obtained MBI films is 500–1500 nm.

The ferroelectric phase of MBI crystals forms a pseudotetragonal lattice at room temperature, as schematically shown in Fig. 2. In the crystal, hydrogen-bonded chains between the molecules are formed either along the $[110]_{tetra}$ or $[1-10]_{tetra}$ directions, in which spontaneous polarization is parallel to either the $[100]_{tetra}$ or $[010]_{tetra}$ directions [26]. The $[001]_{tetra}$ and $[110]_{tetra}$ directions are parallel to the substrate in the fabricated thin films [27]. In the birefringent FFMI measurement, the direction of incident optical polarization is fixed at 45° from the $[001]_{tetra}$ direction, and the external electric field is applied along the $[110]_{tetra}$ direction. Here, we assume that the refractive indices along the $[001]_{tetra}$ and $[110]_{tetra}$ directions are n_x and n_y, respectively.

B. Visualization of domain and domain walls

Figure 3(a) presents the results of birefringent FFMI measurements in the cases of $\Delta T_{||}/T_{||}$ and $\Delta T_{\perp}/T_{\perp}$. We apply a square-wave bias at frequencies of 10–80 Hz with an amplitude of 100 $V_{p.p.}$ between a pair of adjacent stripe-shaped electrodes. A clear contrast between red (positive signal) and blue (negative signal) is observed in both images. It is seen in the $\Delta T_{||}/T_{||}$ image that several striped blue-colored areas with widths of a few tens of micrometers are extended along the $[110]_{tetra}$ direction. The signal amplitudes at the red- and blue-colored areas are roughly the same in the image. This feature is consistent with the observation of ferroelectric domains with antiparallel spontaneous polarizations, as previously described. Meanwhile, we also observe an almost reverse example of the $\Delta T_{||}/T_{||}$ image with regard to the sign in the $\Delta T_{\perp}/T_{\perp}$ image. The observed sign change is reasonable, considering the ellipticity modulation of the elliptically polarized light under $\mathbf{E}_{ext}$, as shown in Fig. 1(c) and Eq. (5).

PFM measurements are conducted with a commercially available scanning probe microscope (Cypher; Oxford instruments) using a conducting tip. Both out-of-plane and in-plane components of spontaneous polarization are measured using vertical-mode PFM and lateral-mode PFM, respectively. Figure 3(b) presents the phase images of the vertical (out-of-plane) and lateral (in-plane) PFM results measured in the same area as Fig. 3(a). A comparison between Figs. 3(a) and 3(b) clearly shows that the FFMI image corresponds to the domain structure, as observed in the PFM image. Since both vertical and lateral PFM images show the phase change between adjacent domains (both out-of-plane and in-plane components of spontaneous polarization are opposite between adjacent domains), it is confirmed that the observed domain structure is composed of antiparallel spontaneous polarization

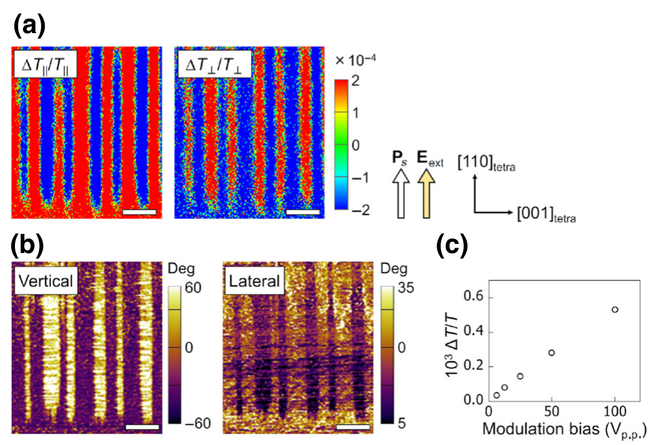

FIG. 3. (a) Birefringent FFMI images measured for a MBI single-crystal thin film at $\lambda = 660$ nm in the cases of $\Delta T_{||}/T_{||}$ (left) and $\Delta T_{\perp}/T_{\perp}$ (right). Scale bars: 20 μm. Directions of the in-plane component of spontaneous polarization ($\mathbf{P}_s$) and the applied electric field ($\mathbf{E}_{ext}$) are shown by white and orange arrows, respectively. (b) Vertical (left) and lateral (right) PFM images measured in the same area as (a), which show the out-of-plane and in-plane components of spontaneous polarization, respectively. Scale bars: 20 μm. (c) Dependence of $\Delta T_{||}/T_{||}$ on the applied modulation bias.

along the $[100]_{tetra}$ or $[010]_{tetra}$ directions [see Fig. 2(a)], as previously reported (i.e., 90° domain wall is not observed in spite of the two-axial ferroelectricity) [27]. These results provide unambiguous evidence that the birefringent FFMI facilitates the visualization of the ferroelectric domain with antiparallel polarizations. Figure 3(c) shows the relationship between $\Delta T_{||}/T_{||}$ and the modulation bias measured for a sample. Evidently, $\Delta T_{||}/T_{||}$ is proportional to the applied modulation bias, corroborating the proposition that the origin of $\Delta T_{||}/T_{||}$ is the Pockels effect, which is the first-order electro-optic effect derived from the lack of inversion symmetry.

C. Wavelength dependence of the birefringent field-modulation signal

To further investigate the electro-optic response of MBI films, we measure the wavelength dependence of $\Delta T_{||}/T_{||}$ and $\Delta T_{\perp}/T_{\perp}$ by changing the light source in the birefringent FFMI technique. We also measure the birefringent field modulation ($\Delta T_{||}/T_{||}$ and $\Delta T_{\perp}/T_{\perp}$) spectra and the polarized transmittance ($T_{||}$ and $T_{\perp}$) spectra using the combination of a monochromator (M25-GT, Bunkokeiki Co.) and a lock-in amplifier (LI 5640; NF Co.).

We first show the ordinary polarized optical absorption spectra, measured using a spectrophotometer (UV-2450; Shimadzu Co.), as shown in Fig. 4(a). The film is transparent over the entire visible region. The absorption band near $\lambda = 283$ nm is due to the $\pi - \pi^*$ transition of the MBI molecule. The absorption along $[110]_{tetra}$ is much stronger than that along $[001]_{tetra}$ because the transition dipole is parallel to the molecular plane (Fig. S2 within the Supplemental Material [30]). This feature is the origin of the larger n_y (along $[110]_{tetra}$) compared with that of n_x (along $[001]_{tetra}$), as discussed later.

Figure 4(b) presents the $T_{||}$ and $T_{\perp}$ spectra of the MBI films. We clearly observe an oscillation in the $T_{||}$ and $T_{\perp}$ spectra in the visible-wavelength region. The oscillation is due to the variation in ellipticity of the outgoing elliptically polarized light, as schematically shown at the top of Fig. 4(b). These spectra can be fitted well by Eqs. (2) and (3) by considering the Sellmeier dispersion formula for n_x and n_y (see Fig. S3 within the Supplemental Material [30]). The fitting results of the $T_{||}$ and $T_{\perp}$ spectra indicate that the birefringence, $n_y - n_x$, is estimated to be 0.39 at $\lambda = 600$ nm. We also roughly estimated the refractive indices from the interference of the T_y and T_x spectra as $n_y = 2.11$ and $n_x = 1.65$ at $\lambda = 600$ nm, respectively (Fig. S4 within the Supplemental Material [30]). The observed birefringence of MBI is much larger than the reported value for $LiNbO_3$ (<0.1) [31,32]. The observed large anisotropy is ascribed to the characteristic feature of molecular crystals, in which the planar π-conjugated molecules are arranged almost parallel to each other (Fig. 2).

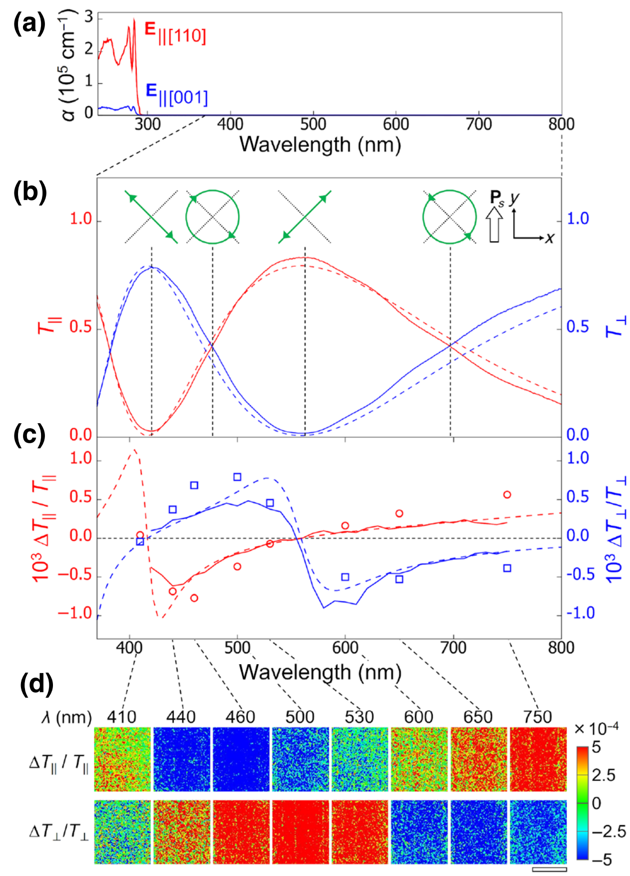

FIG. 4. (a) Absorption spectra of a MBI thin film measured with polarized light along [110] (red) and [001] (blue). Vertical axis is the absorption coefficient calculated from the absorbance and the film thickness. (b) Wavelength dependence of $T_{\perp}$ (blue curve) and $T_{||}$ (red curve). (c) Wavelength dependence of $\Delta T_{\perp}/T_{\perp}$ and $\Delta T_{||}/T_{||}$, as measured by FFMI (red open circles and blue open squares, respectively) and by field-modulation spectroscopy (red and blue solid curves, respectively). Theoretical curves are also shown for $\Delta T_{\perp}/T_{\perp}$ (blue dashed curve) and $\Delta T_{||}/T_{||}$ (red dashed curve). (d) FFMI images measured at various wavelengths with parallel- (top) and crossed-Nicols (bottom) polarizers, respectively. Scale bar: 10 μm.

Figure 4(c) shows the measured $\Delta T_{||}/T_{||}$ and $\Delta T_{\perp}/T_{\perp}$ spectra. Clear sign changes are observed near 560 nm from negative (positive) to positive (negative) in the $\Delta T_{||}/T_{||}$ ($\Delta T_{\perp}/T_{\perp}$) spectra. Figure 4(d) shows the FFMI images obtained at various wavelengths. The wavelength dependence of $\Delta T_{||}/T_{||}$ and $\Delta T_{\perp}/T_{\perp}$ obtained by the FFMI images shows the same tendency as that of the $\Delta T_{||}/T_{||}$ and $\Delta T_{\perp}/T_{\perp}$ spectra [Fig. 4(c)]. The strong wavelength dependence of the electro-optic effect, as observed in the MBI films, can be ascribed to the large birefringence (see Fig. S5 within the Supplemental Material [30]). The obtained $\Delta T_{||}/T_{||}$ and $\Delta T_{\perp}/T_{\perp}$ spectra are well fitted by Eqs. (4)–(6) [Fig. 4(c)], assuming the same parameters are used to fit the results of the $T_{||}$ and $T_{\perp}$ spectra. From the results, the

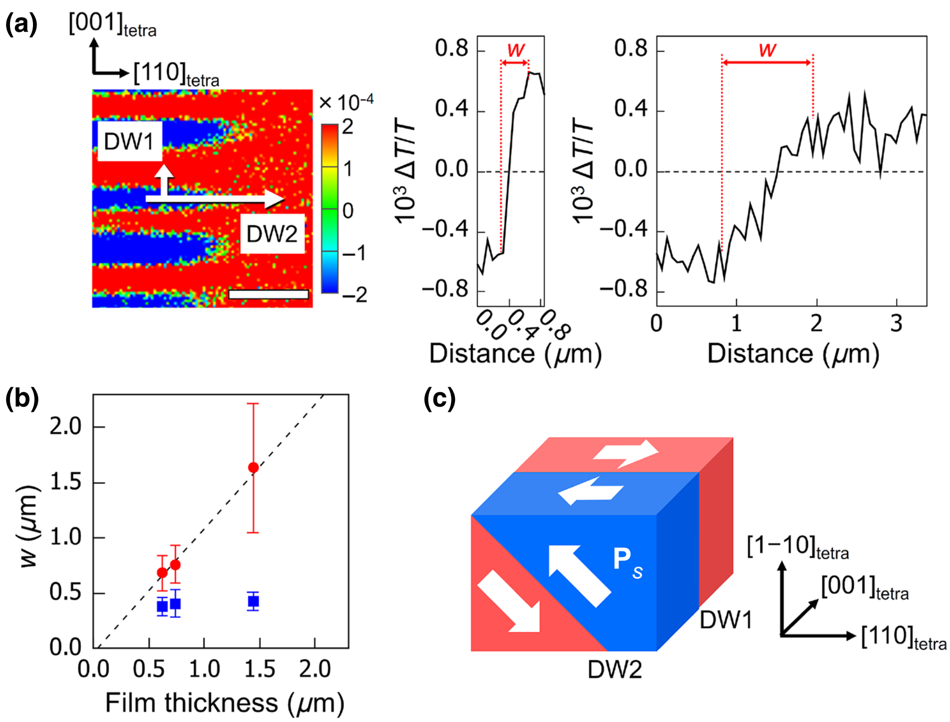

FIG. 5. (a) FFMI image of a MBI film (left) and line profiles of FFMI signal across DW1 (center) and DW2 (right), respectively. White arrows in the FFMI image indicate lines along which the signal intensity is plotted. Scale bar: 2 μm. (b) Film-thickness dependence of the spatial width (w) for the FFMI signal variation plotted for DW1 (blue square) and DW2 (red circle), respectively. Dashed line is a linear fit for DW2. (c) Schematics of the three-dimensional structure of ferroelectric domains in MBI films.

electro-optic coefficient of $\partial(n_y - n_x)/\partial E_{\text{ext}}$ is estimated to be approximately 10 pm/V at $\lambda = 600$ nm.

D. On the three-dimensional orientation of the domain walls

Figure 3(a) shows that the observed domain walls along $[110]_{\text{tetra}}$ (DW1) tend to be straight and much longer than those along $[001]_{\text{tetra}}$ (DW2). We focus on the different features of these two types of domain walls and analyze the profile of the FFMI signal across DW1 and DW2 [Fig. 5(a)]. We find that the intensity of the FFMI signal for DW2 shows a gradual change at a distance of 1.4 μm, whereas DW1 shows a steep signal change with a distance of less than 0.5 μm. It has been reported that the magnitude of the FFMI signal indicates the domain structure in the depth direction because of the use of transmitted light [23,24]. When opposite domains overlap in the depth direction (domain walls are inclined from the normal to the substrate), the electro-optic response in each domain cancels out, which causes relatively weak signals around the domain boundary. Thus, the relatively weak signal region around DW2 should indicate tilting of the domain wall. We also find that the spatial width (w) for the FFMI signal variation around DW2 is roughly proportional to the film thickness, with a slope of approximately 48°; meanwhile, w for DW1 is almost equal to the diffraction limit of light and does not depend on the film thickness [Fig. 5(b)]. This result indicates that DW2 is tilted by 48° from the substrate, whereas DW1 is almost perpendicular to the substrate. As $\mathbf{P}_s$ in the MBI film is tilted from the substrate by 45° in the $(001)_{\text{tetra}}$ plane, according to the crystal orientation, it is confirmed that DW1 is parallel to $\mathbf{P}_s$, whereas the orientation of DW2 is uncertain. There are two possibilities, parallel or perpendicular to $\mathbf{P}_s$. We consider that DW2 should also be parallel to $\mathbf{P}_s$ because of the electrical neutrality without bound charges. Thus, we consider that both DW1 and DW2 should be neutral domain walls [Fig. 5(c)]. However, the observed respective domains are stripelike, extended along the $[110]_{\text{tetra}}$ direction (along DW1), which implies that the interfacial energy of DW2 is much larger than that of DW1. It is most likely that protons in hydrogen bonds around DW2 should be unstable, because DW2 is formed across the one-dimensional hydrogen-bonded chains along the $[110]_{\text{tetra}}$ and $[1-10]_{\text{tetra}}$ directions [see Fig. 2(a)].

IV. CONCLUSION

We develop a birefringent FFMI technique that allows the visualization of ferroelectric domains and domain walls in transparent ferroelectric thin films with a parallel- and crossed-Nicol-polarized optical microscope. The technique is based on measuring the difference in the ellipticity of polarized light transmitted by ferroelectric domains of opposite orientation in applied electric fields, a manifestation of the Pockels effect. We utilize a CMOS area image sensor to obtain difference microscopy images between those obtained under forward electric fields and reverse electric fields, sensitively and collectively, at once. This technique is applicable to most ferroelectric materials, including transparent inorganic and organic materials, unlike the previously reported FFMI, which utilizes the electroabsorption effect and is only applicable to colored ferroelectric materials. Using the birefringent FFMI, we successfully visualize the structure of stripelike domains and their antiparallel (180°) domain walls in single-crystal films of hydrogen-bonded-type molecular ferroelectrics of MBI. We find that the birefringent FFMI signal exhibits a strong wavelength dependence, accompanied by a sign change, the feature of which can be ascribed to the highly anisotropic nature of organic-molecule-based ferroelectrics. The use of transmitted light also enables the analysis of domain structures in the depth direction, revealing that two types of domain walls are formed: one that is perpendicular to the film plane and the other tilted from the film plane. Such a three-dimensional understanding of domain wall structure should be useful for developing domain engineering in ferroelectric materials.

The birefringent FFMI technique is simple, as it is based on a polarized optical microscope using an incoherent light source from LEDs or monochromatized light. Nonetheless, the use of area image sensors facilitates the visualization of the spatial distribution of the electro-optic response of the samples over a wide area in a short period of time. From the features and results presented above, we believe that the birefringent FFMI should provide a useful means for investigating ferroelectric domain structures and electro-optic effects, which is useful for understanding and controlling the further development of electro-optic devices based on ferroelectrics.

ACKNOWLEDGMENTS

This work is partially supported by JSPS KAKENHI (Grants No. JP19H02579, No. JP19H02587, and No. JP18J22030) and by JST CREST (Grant No. JPMJCR18J2), Japan.

[1] M. Cardona, Optical properties and band structure of $SrTiO_3$ and $BaTiO_3$, Phys. Rev. **140**, A651 (1965).

[2] M. Okuyama, T. Usuki, and Y. Hamakawa, Epitaxial growth of ferroelectric PLZT thin film and their optical properties, Appl. Phys. **21**, 339 (1980).

[3] L. Arizmendi, Photonic applications of lithium niobate crystals, Phys. Status Solidi. (a) **201**, 253 (2004).

[4] D. Damjanovic, Ferroelectric, dielectric and piezoelectric properties of ferroelectric thin films and ceramics, Rep. Prog. Phys. **61**, 1267 (1998).

[5] G. Catalan, J. Seidel, R. Ramesh, and J. F. Scott, Domain wall nanoelectronics, Rev. Mod. Phys. **84**, 119 (2012).

[6] W. J. Merz, Domain formation and domain wall motions in ferroelectric BaTiO3 single crystals, Phys. Rev. **95**, 690 (1954).

[7] V. Gopalan and T. E. Mitchell, In situ video observation of 180° domain switching in $LiTaO_3$ by electro-optic imaging microscopy, J. Appl. Phys. **85**, 2304 (1999).

[8] M. Müller, E. Soergel, and K. Buse, Visualization of ferroelectric domains with coherent light, Opt. Lett. **28**, 2515 (2003).

[9] C. Qiu, B. Wang, N. Zhang, S. Zhang, J. Liu, D. Walker, Y. Wang, H. Tian, T. R. Shrout, Z. Xu, L.-Q. Chen, and F. Li, Transparent ferroelectric crystals with ultrahigh piezoelectricity, Nature **577**, 350 (2020).

[10] S. E. Cummins and T. E. Luke, A new method of optically reading domains in bismuth titanate for display and memory applications, IEEE Trans. Electron Devices **18**, 761 (1971).

[11] A. Gruverman and S. V. Kalinin, Piezoresponse force microscopy and recent advances in nanoscale studies of ferroelectrics, J. Mater. Sci. **41**, 107 (2006).

[12] E. Soergel, Piezoresponse force microscopy (PFM), J. Phys. D: Appl. Phys. **44**, 46 (2011).

[13] Q. Zhang, S. Prokhorenko, Y. Nahas, L. Xie, L. Bellaiche, A. Gruverman, and N. Valanoor, Deterministic switching of ferroelectric bubble nanodomains, Adv. Funct. Mater. **29**, 1808573 (2019).

[14] G. Tian, W. Yang, X. Song, D. Zheng, L. Zhang, C. Chen, P. Li, H. Fan, J. Yao, D. Chen, Z. Fan, Z. Hou, Z. Zhang, S. Wu, M. Zeng, and X. Gao, Manipulation of conductive domain walls in confined ferroelectric nanoislands, Adv. Funct. Mater. **29**, 1807276 (2019).

[15] Y. Cho, A. Kirihara, and T. Saeki, Scanning nonlinear dielectric microscope, Rev. Sci. Instrum. **67**, 2297 (1996).

[16] C. Gao, F. Duewer, Y. Lu, and X.-D. Xiang, Quantitative nonlinear dielectric microscopy of periodically polarized ferroelectric domains, Appl. Phys. Lett. **73**, 1146 (1998).

[17] Y. Uesu, S. Kurimura, and Y. Yamamoto, Optical second harmonic images of 90° domain structure in $BaTiO_3$ and periodically inverted antiparallel domains in $LiTaO_3$, Appl. Phys. Lett. **66**, 2165 (1995).

[18] S. A. Denev, T. T. A. Lummen, E. Barnes, A. Kumar, and V. Gopalan, Probing ferroelectrics using optical second harmonic generation, Am. Ceram. Soc. **94**, 2699 (2011).

[19] S. C-Hertel, H. Bulou, R. Hertel, G. Taupier, K. D. H. Dorkenoo, C. Andreas, J. Guyonnet, I. Gaponenko, K. Gallo, and P. Paruch, Non-Ising and chiral ferroelectric domain walls revealed by nonlinear optical microscopy, Nat. Commun. **8**, 15768 (2017).

[20] M. Sotome, N. Kida, S. Horiuchi, and H. Okamoto, Visualization of ferroelectric domains in a hydrogen-bonded molecular crystal using emission of terahertz radiation, Appl. Phys. Lett. **105**, 041101 (2014).

[21] M. Sotome, N. Kida, S. Horiuchi, and H. Okamoto, Terahertz radiation imaging of ferroelectric domain topography in room-temperature hydrogen-bonded supramolecular ferroelectrics, ACS Photonics **2**, 1373 (2015).

[22] M. Sotome, N. Kida, Y. Kinoshita, H. Yamakawa, T. Miyamoto, H. Mori, and H. Okamoto, Visualization of a nonlinear conducting path in an organic molecular ferroelectric by using emission of terahertz radiation, Phys. Rev. B **95**, 241102 (2017).

[23] Y. Uemura, S. Arai, J. Tsutsumi, S. Matsuoka, H. Yamada, R. Kumai, S. Horiuchi, A. Sawa, and T. Hasegawa, Field-Modulation Imaging of Ferroelectric Domains in Molecular Single-Crystal Films, Phys. Rev. Appl. **11**, 014046 (2019).

[24] Y. Uemura, S. Arai, J. Tsutsumi, S. Matsuoka, H. Yamada, R. Kumai, S. Horiuchi, A. Sawa, and T. Hasegawa, Ferroelectrics field modulation imaging: A useful technique for domain and domain-wall observations, Ferroelectrics **556**, 37 (2020).

[25] S. Horiuchi and S. Ishibashi, Hydrogen-Bonded small-molecular crystals yielding strong ferroelectric and anti-ferroelectric polarizations, J. Phys. Soc. Jpn **89**, 051009 (2020).

[26] S. Horiuchi, F. Kagawa, K. Hatahara, K. Kobayashi, R. Kumai, Y. Murakami, and Y. Tokura, Above-room-temperature ferroelectricity and antiferro-electricity in benzimidazoles, Nat. Commun. **8**, 1308 (2012).

[27] Y. Noda, T. Yamada, K. Kobayashi, R. Kumai, S. Horiuchi, F. Kagawa, and T. Hasegawa, Few-volt operation of printed organic ferroelectric capacitor, Adv. Mater. **27**, 6475 (2015).

[28] T. Kawasaki, T. Terashima, S. Suzuki, and T. Takada, AC surface discharge on dielectric materials observed by advanced pockels effect technique, J. Appl. Phys. **76**, 3724 (1994).

[29] A. Kumada, M. Chiba, and K. Hidaka, Potential distribution measurement of surface discharge by pockels sensing technique, J. Appl. Phys. **84**, 3059 (1998).

[30] See the Supplemental Material at http://link.aps.org/supplemental/10.1103/PhysRevApplied.14.024060 for optical micrographs of a single-crystal thin film of MBI and detailed information on DFT calculations and spectrum analyses.

[31] D. S. Smith, H. D. Riccius, and R. P. Edwin, Refractive indices of lithium niobite, Opt. Commun. **17**, 332 (1976).

[32] M. Aillerie, M. D. Fontana, F. Abdi, and C. Carabatos-Nedelec, Influence of the temperature-dependent spontaneous birefringence in the electro-optic measurements of $LiNbO_3$, J. Appl. Phys. **65**, 2406 (1989).